CEAS Space Journal
https://doi.org/10.1007/s12567-024-00561-z

ORIGINAL PAPER

Aerothermal characterization of the CALLISTO vehicle during descent

Tobias Ecker[1] · Moritz Ertl[1] · Josef Klevanski[2] · Sven Krummen[3] · Etienne Dumont[3]

Received: 3 July 2024 / Revised: 7 August 2024 / Accepted: 7 August 2024

Abstract
Aerothermal loads are a design driving factor during launcher development as the thermal loads directly influence thermal protection system (TPS) design and successively the possible flight trajectory and mission profiles. Recent developments in reusable launch vehicles (RLV) (e.g. SpaceX, Blue Origin) have added the dimension of refurbishment to the challenges the thermal design must consider. With the current European launcher roadmap moving towards a reusable first stage aerothermal loads may significantly change. The CALLISTO vehicle is a flight demonstrator for future reusable launcher stages and their technologies developed by a tri-national consortium and planned to fly in 2025. For this vehicle the highest heat fluxes are mainly due to heating from hot exhaust gases and heated air in the proximity of the aft bay and on the exposed structures like legs and fins. In the presented study we conducted computational fluid dynamics (CFD) studies to determine the aerothermal loads on the vehicle during descent through the landing approach corridor for both phase B and phase C aeroshapes. A defining difference to previous aerothermal databases (ATD) is that the CALLISTO demonstrator is planned to execute a series of test flights with different energy levels, as well as a final demo flight. This leads to an large parameter space the final aerothermal database needs to cover. The database development is described in detail and analysed for integral and local loads, as well as interpolation uncertainties. The final phase C database allows interpolation of interface heatfluxes for the entire flight domain (Mach number, density ρ) at varying angle of attack (AoA). Further the sensitivity of the plume-vehicle interaction to angle of attack, chemistry, thrust vector control (TVC) and engine throttling are investigated for a critical Mach number indicating further areas of improvement for future databases.

Keywords Retropropulsion · Reusable launcher · CFD · Thermal loads · Plume

1 Introduction

Aerothermal loads are a design driving factor during launcher development as the thermal loads directly influence TPS design and trajectory. Recent developments in reusable launch vehicles (RLV) (e.g. SpaceX, Blue Origin) have added the dimension of refurbishment to the challenges the thermal design must consider.

For classical disposable launchers like the Ariane 5 [1] and 6, the TITAN 3C [2], but also the space shuttle launch and reentry [3], the heat flux due to base heating during ascent needs to be considered for aft thermal protections system (TPS) and structural design. In all these configurations the use of solid rocket boosters lead to a significant increase in heat flux due to plume radiation. With the current European long-term strategy [4, 5] moving from the LH2/LOX powered Vinci and Vulcain 2.1 on Ariane 6, supported by solid rocket boosters, to a single-engine concept (Prometheus [6, 7]) based on LCH4/LOX with

✉ Tobias Ecker
Tobias.Ecker@dlr.de

Moritz Ertl
Moritz.Ertl@dlr.de

Josef Klevanski
Josef.Klevanski@dlr.de

Sven Krummen
Sven.Krummen@dlr.de

Etienne Dumont
Etienne.Dumont@dlr.de

1 Institute of Aerodynamics and Flow Technology, German Aerospace Center (DLR), Bunsenstr. 10, 37073 Göttingen, Germany

2 Institute of Aerodynamics and Flow Technology, German Aerospace Center (DLR), Linder Höhe, 51147 Köln, Germany

3 Institute of Space Systems, German Aerospace Center (DLR), Robert-Hooke-Strasse 7, 28359 Bremen, Germany

no solid rocket boosters on a future European launcher-aerothermal loads may significantly change.

The CALLISTO (Cooperative Action Leading to Launcher Innovation in Stage Toss-back Operations) vehicle is a flight demonstrator for future reusable launcher stages and their technologies. The program involves three countries and their space organizations: CNES for France, DLR for Germany and JAXA for Japan. The first tests will be conducted in 2025 from CSG, Europe's Spaceport. This program includes products and vehicle design, ground segment set up, and post-flight operations for vehicle recovery and subsequent reuse [8–11]. It is a stepping stone on the European roadmap towards large-scale demonstrators like THEMIS [12] and subsequently full scale launchers such as Ariane next/7 [6, 7] and planned to fly in 2025.

For the CALLISTO vehicle the highest heat fluxes are mainly due to heating from hot exhaust gases and heated air in proximity to the aft bay and on the exposed structures such as legs and fins. The development of the plume extension is different for the considered re-entry, when compared to Falcon 9, or the studies presented in [13–15]. As shown by Dumont et al. [16] the plume remains relatively concentrated at the aft end of the vehicle due to high atmospheric pressure and only very low fractions of actual exhaust gas species enclosing the vehicle. For the purpose of systems engineering and product development detailed aerothermal loads estimates are required. In the current study we conducted computational fluid dynamics (CFD) studies to determine the aerothermal loads on the vehicle during descent through the landing approach corridor. The CALLISTO general flight profile, vehicle configuration, vehicle aeroshape evolution and the relevant thermal interfaces as well as the flight domain and its changes from phase B to C are described in detail. The engine model and thermodynamic modelling approach are described and applied to preparatory 2D studies of the engine plume. A defining difference to aerothermal characterisation of other configurations previously studied (RETALT/RETPRO/Falcon9) [13, 17–19] is that the CALLISTO demonstrator is planned to execute a series of test flights with different energy levels, as well as a final demo flight [10] which leads to a large parameter space the final database needs to cover. Based on these premises the database development for vehicle phase B and phase C aeroshapes are described and analysed for some of the most prominent interfaces. Further the sensitivity of the plume-vehicle interaction to angle of attack (AoA), chemistry, thrust vector control (TVC) and engine throttling are investigated. For the purpose of this study, the main focus is on the closed leg configuration, more details for the configuration right before touchdown can be found in Ertl et al. [20]. Further comparisons of the impact of aeroshape progression in later project stages are shown in Ertl et al. [21].

2 CALLISTO configurations, aeroshape and flight domain

2.1 General CALLISTO flight profile

The CALLISTO vehicle and flight experiment aim to demonstrate the technologies and capabilities to realize a VTVL first-stage launcher. The basic vehicle architecture is outlined in Fig. 1. A few selected interfaces are shown in the drawing (from left to right): base-plate, aft-bay, automatic landing system (ALS), LH_2 tank (LH2), LOX tank (LOX), vehicle equipment bay (VEB), flight control system aerodynamic (FCSA) and the fairing. As an experimental vehicle, flight conditions are similar for certain flight phases but not the same as the ones encountered by full-scale VTVL first-stage launcher (e.g. Falcon 9). Differences arise in altitude, maximum Mach number and realizable trajectory/flight parameters. The main difference is the lack of a supersonic retro-propulsion phase as encountered in [13, 22].

The altitude and Mach number during flight, as well as heat fluxes in terms of Nusselt number on selected interfaces (as marked in Fig. 1) for a representative trajectory [23] are shown in Fig. 2 based on preliminary 2D calculations. The Nusselt number is defined as:

$$Nu = \frac{qL}{k * (T_{cc} - T_{\infty})} \tag{1}$$

where q is the heat flux (units: W/m^2) , L the characteristic length (d = 1.1 m), k the thermal conductivity (units: kg m s^{-3} K^{-1}) of air and T_{cc} the combustion chamber temperature (units: K) and T_{∞} the wall temperature (units: K).

It can be seen that there are two main differences when compared to a classical expendable launcher: First, aside from the heat flux on the baseplate which is due to convective base heating, the heat flux due to aerodynamic heating is minimal. This is due to the low supersonic and subsonic Mach numbers during the ascent and ballistic descent. The heat flux on the fairing of Ariane 5 is of the order of 10–20

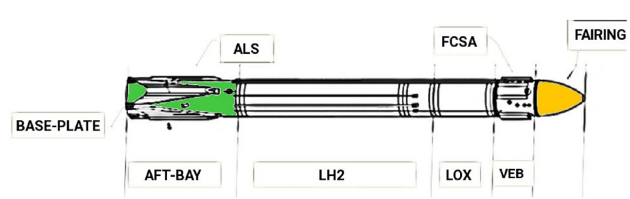

Fig. 1 Overview of CALLISTO vehicle architecture (adapted from [23])

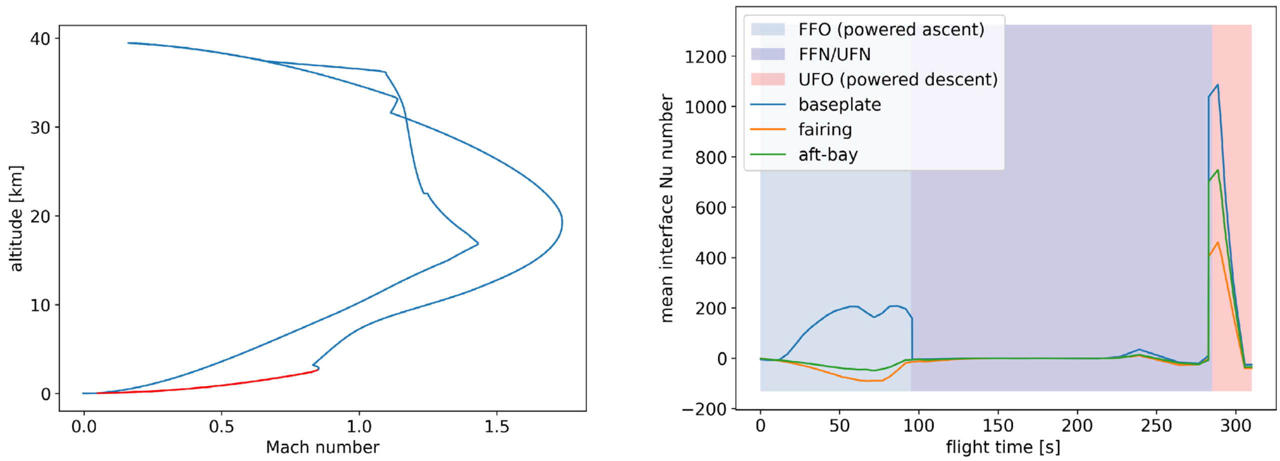

(a) Representative trajectory. Red line marks the powered descent phase.

(b) Nu number on fairing, aft-bay and baseplate during example flight profile. (based on 2D model, T_w = const. = 300 K)

Fig. 2 Representative CALLISTO flight profile and preliminary aerothermal characteristics (early Phase A)

kW/m^2 [24], while for the CALLISTO vehicle it is negative until the retro-boost maneuver. The second difference is the occurrence of high heat fluxes during the retro boost maneuver, leading to thermal loads 2–4 times higher than occurring during forward flight. More information on the CALLISTO flight profile and demonstration flight objectives can be found in [11, 25].

During flight four main flight regimes are present: powered vehicle forward flight, ballistic vehicle forward flight, ballistic vehicle return flight and vehicle retro boost during return flight. During the actual flight various vehicle attitudes (angle of attack, roll angle etc.) are possible. During forward flight the hot exhaust gases are entrained into the recirculation zone at the base of the vehicle, leading to high convective heat fluxes during powered ascent. The ballistic phases have no significant aerothermal implications due to the low Mach numbers of CALLISTO flight profile. This flight regime will be more important for large-scale demonstrators like THEMIS [12] which will reach higher Mach numbers and altitudes at a full-scale flight envelope [4]. The interaction between the exhaust plume, the oncoming air and the vehicle leads to significantly higher heat fluxes, making this the flight phase with the highest thermal loads.

2.2 CALLISTO vehicle configurations

During the descent trajectory multiple configurations with regards to vehicle external parts (FCS/A: aerodynamic control surfaces, landing legs) and ground influence exists. Due to the multitude of required calculations, calculations of non-critical points of the flight domain are conducted by using a simplified 2D-axisymmetric outer mold line. An overview of the considered configurations is given in Table 1 and visualized at the example of the phase B geometry in Fig. 3.

Table 1 Configurations considered for the aerothermal loads during reentry

Configuration	FCS/A status	Legs status	Engine status
UFO (2D)	NA	Folded	Active
UFO	Unfolded	Folded	Active
UUO	Unfolded	Unfolded	Active
UUO ground	Unfolded	Unfolded	Active

2.3 CALLISTO aeroshape evolution

During the project, the CALLISTO aeroshape has changed in various ways. A comparison of previous outer mold lines with the shape CAL1B (phase *B* shape) can be found in [23]. The evolution of the aeroshape from a late phase *A* (CAL1N) to the phase C aeroshape (CAL1B) is shown in Fig. 4. Previous aeroshapes considered different diameters and aft-bay shapes [16]. From Phase *B* onwards the shape changes were mostly limited to detailed design of legs, cable ducts and piping as well as changes due to TPS application and product design. The major difference for CAL1C is the addition of cable ducts, piping and TPS. For this paper only aeroshapes CAL1B and CAL1C are considered. The aeroshape evolution and related aerodynamic properties are further detailed in [21, 26]. The first project wide used aerothermal database was introduced with the CAL1B aeroshape. The vehicle length is 13.455 m for the CAL1C aeroshape and 1.1 m diameter [20].

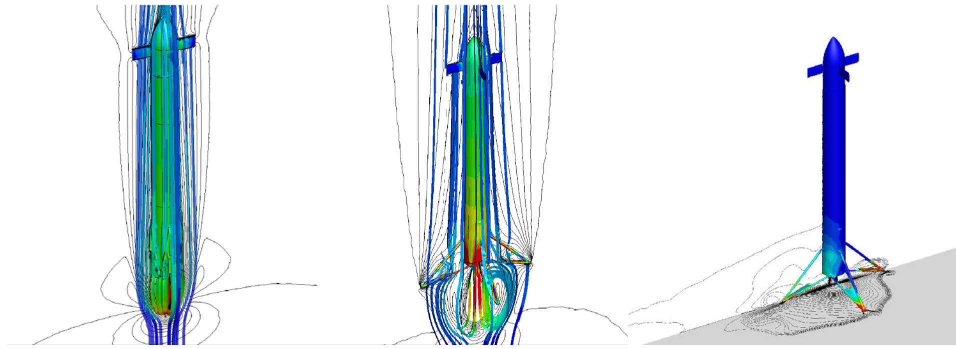

(a) UFO flight (b) UUO flight (c) UUO on ground

Fig. 3 Applicable configurations demonstrated for the CAL1B aeroshape. Streamlines are colored (red: hot, blue:cold) by gas temperature. Wall colors indicates heatflux

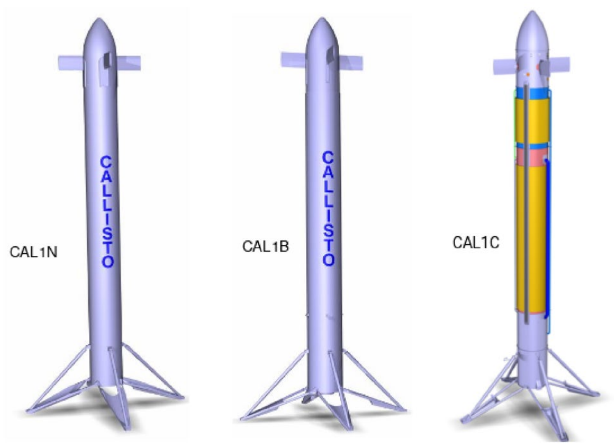

Fig. 4 CALLISTO aeroshape evolution

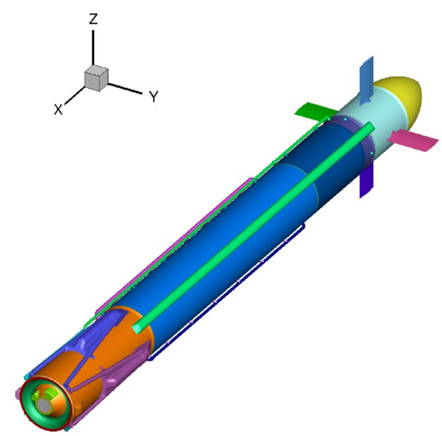

Fig. 5 CALLISTO CAL1C vehicle: overview of all distinct thermal and aerodynamic interfaces

2.4 CALLISTO thermal interfaces

For use in the CALLISTO design process and loads definition, thermal interfaces (tanks, legs, etc.) for the entire vehicle were defined. While the CAL1B aeroshape had 15 thermal interfaces, the CAL1C aeroshape had more than 50 thermal interfaces. The number of interfaces varies by configuration, with more interfaces being present for the legs open (e.g. UUO) configuration. A graphic of the thermal interfaces is shown in Fig. 5. The fairing and legs assemblies have multiple thermal interfaces not pictured here which are described more in detail in references [20, 27]. Additional sub-zoning of interfaces was performed for interfaces with locally high loads during post-processing based on system design and product design requirements distributed via systems engineering [28]. For example, the fairing was zoned into 5 sections to allow better sizing of the TPS [29].

3 CFD solver and models

All numerical investigations in the framework of the present study were performed with the hybrid structured/unstructured DLR Navier-Stokes solver TAU [30, 31], which is validated [32, 33] for a wide range of steady and unsteady sub-, trans [34]- and hypersonic [35] flow cases. The TAU code is a second order finite-volume solver for the Euler and Navier–Stokes equations in the integral form using eddy-viscosity, Reynolds-stress or detached- and large eddy simulation for turbulence modelling. An improved Advection Upstream Splitting Method (AUSMDV [36]) flux vector splitting scheme was applied together with Monotonic Upstream-centered Scheme for Conservation Laws (MUSCL [37]) gradient reconstruction to achieve second-order spatial accuracy. TAU allows for the computation of flows in thermal and chemical equilibrium and non-equilibrium. For cases with chemical non-equilibrium (e.g. in a rocket combustion chambers [38]) the reacting flow can be modeled using finite rate chemistry [39] or flamelet modelling.

3.1 Engine conditions

The Reusable Sounding Rocket (RSR) engine used for CALLISTO is developed by JAXA in cooperation with Mitsubishi Heavy Industries (MHI) and is based on LOX/LH_2 fuel. The RSR engine uses an expander bleed cycle, is restartable and throttable between 40 and 100 % nominal thrust [40]. Further studies demonstrated an increased throttle range between 21 and 109 % [41]. By-passing the turbopumps allows operation in "idle mode" [11]. A summary of the RSR engine which will be used in a modified version for CALLISTO can be found in [42]. For CALLISTO operation up to 110 % thrust level is planned. All calculations or CAL1B are at nominal thrust level, while for CAL1C-based data 110% thrust level was assumed (see Table 2, unless specified otherwise).

3.2 Thermo-chemical models for retro-propulsion plumes

In order to study the influence of turbulence modeling and post combustion within the plume, a brief 2D study on a subsonic retropropulsion flow field was conducted during an early phase *B* study. For an approximate 2D configuration based on CAL1B geometry [23] the influence of the single equation Spalart-Allmaras [44], two-equation (k-ω) Menter SST [45] and 5 equation Reynolds Stress Models (RSM) [46, 47] turbulence models were investigated along with plume chemistry based on frozen thermally perfect gas mixture and finite rate chemistry modelling of the plume post-combustion. The finite rate chemistry model used in this study is the reduced Jachimowski mechanism [14, 48].

The chemistry as well as the thermodynamic properties of the engine exhaust plume can be modelled in various ways. Four immediate approaches to model the thermo-chemical process from engine to plume can be defined: (1: FR-γ) the use of a perfect gas to describe both the air and the exhaust. This approach will lead to unphysical exit temperatures and flow features and cannot be recommended. (2: FR-CC) Two thermally perfect gas mixtures, one for the air and one for the combustion products, frozen at the combustion chamber. This approach does not take into account thermal equilibrium or no-equilibrium within the nozzle and therefore also produces unrealistic exit temperatures, gas composition and isentropic coefficient. (3: FR-N) Two thermally perfect gas mixtures as before, but frozen at the nozzle exit. This produces realistic engine exit conditions as the postcombustion for lean H_2/LOX engines is limited. At last the (4: NEQ-CC) approach to apply chemical non-equilibrium, basically modelling the reactive flow in the entire domain. This approach is the most realistic approach as it uses the least amount of assumptions. However, it is computationally expensive. An overview of the described modeling approaches is given in Table 3. In all cases it is assumed that chemical equilibrium is present at engine chamber conditions (see Table 2) based on NASA CEA [49] results (Table 4).

While for supersonic retro-propulsion, the plume shape seems to be somewhat less sensitive to the turbulence modelling [13, 22, 50] larger differences appear for the subsonic case [51]. For this study, we investigated the influence of thermodynamic modelling for two of the engine thermodynamic approaches (FR-CC and NEQ-CC) and different turbulence models. Equilibrium species concentrations and temperature are calculated using NASA CEA [49] for the engine conditions given in Table 2. Except for when full

Table 2 Engine conditions [40, 42, 43]

Condition	110 %	Nominal (100 %)	40 %	20 %	Idle
Thrust	44 kN	40 kN	16 kN	8 kN	ND
Specific impulse (sea level)	ND	320 s	270 s	ND	ND
Mixture ratio	ND	6	6.2	ND	ND
Chamber pressure	ND	34 bar	16 bar	ND	ND
Chamber temperature	Approx. 3500 K	ND	ND	ND	ND

ND: not disclosed

Table 3 Possible chemistry models

Name	Chamber (CC)	Nozzle (N)	Plume	Thermodynamic modell
Constant gamma gas (FR-γ)	EQ	FR	FR	Perfect gas ($\gamma = 1.14$)
Frozen gas (FR-CC)	EQ	FR	FR	2 Thermally perfect gas mixtures
Frozen gas (FR-N)	EQ	EQ	FR	2 Thermally perfect gas mixtures
Full chemistry (NEQ-CC)	EQ	NEQ	NEQ	Mixture thermally perfect gases

(FR: frozen, EQ: chemical equilibrium, NEQ: chemical non-equilibrium modelled using finite rate chemistry)

Table 4 Case matrix

Turbulence modell	FR-CC	NEQ-CC	References
Spalart-Allmaras original (SAO)	x	x	[44]
kω Menter-SST	x	x	[45]
Reynolds Stress Modell (RSM) Wilcox	x	x	[46]
Reynolds Stress Modell (RSM-SSG) SSG		x	[47]

chemistry is considered, air is assumed to be a thermally perfect gas of frozen composition (Y_{N_2}: 0.752, Y_{O_2}: 0.2315, Y_{Ar}: 0.0128, Y_{CO_2}: 3.5e−5). Both thermodynamic properties and transport properties are converted from the CEA databases for use in DLR TAU.

The results are visualized for the plume temperature in Fig. 6. The plume shape and temperature distribution shows that both post-combustion and turbulence model can play a large role in the (subsonic) retro-propulsion plume flow field. However, compared to Kerosene or Methane, post-combustion is limited for hydrogen-fueled engines. For the centerline both the temperature and OH mass fraction as an indicator of post combustion are shown in Fig. 7. Based on the temperature distribution on the centerline, the plume length can be between two to four reference diameters (d=1.1m), with the two equation turbulence models and the RSM turbulence model predicting a significantly longer plume length. Naturally, the OH mass fraction is highest in the stagnation region between the plume and oncoming flow. The temperature increase on the centerline is approximately 500 K when compared to the frozen gas model. Other modelling approaches were considered and tested and as a good compromise FR-N was choosen for all successive calculations (unless otherwise noted). Regardless of the outcome of the turbulence study, lacking further experimental validation, the Spalart-Allmaras (SA) turbulence model [44] is used as the baseline for all future calculations due to its inherent robustness for application in large flight parameter spaces.

4 Aerothermal database for systems engineering during phase B and C

In this section, we describe the general approach to generating aerothermal data for the CALLISTO aerothermal databases. The databases are big in terms of parameter space (configurations, flight conditions) as CALLISTO is expected to execute a series of test flights with different energy levels, as well as a final demo flight. This section is split up in

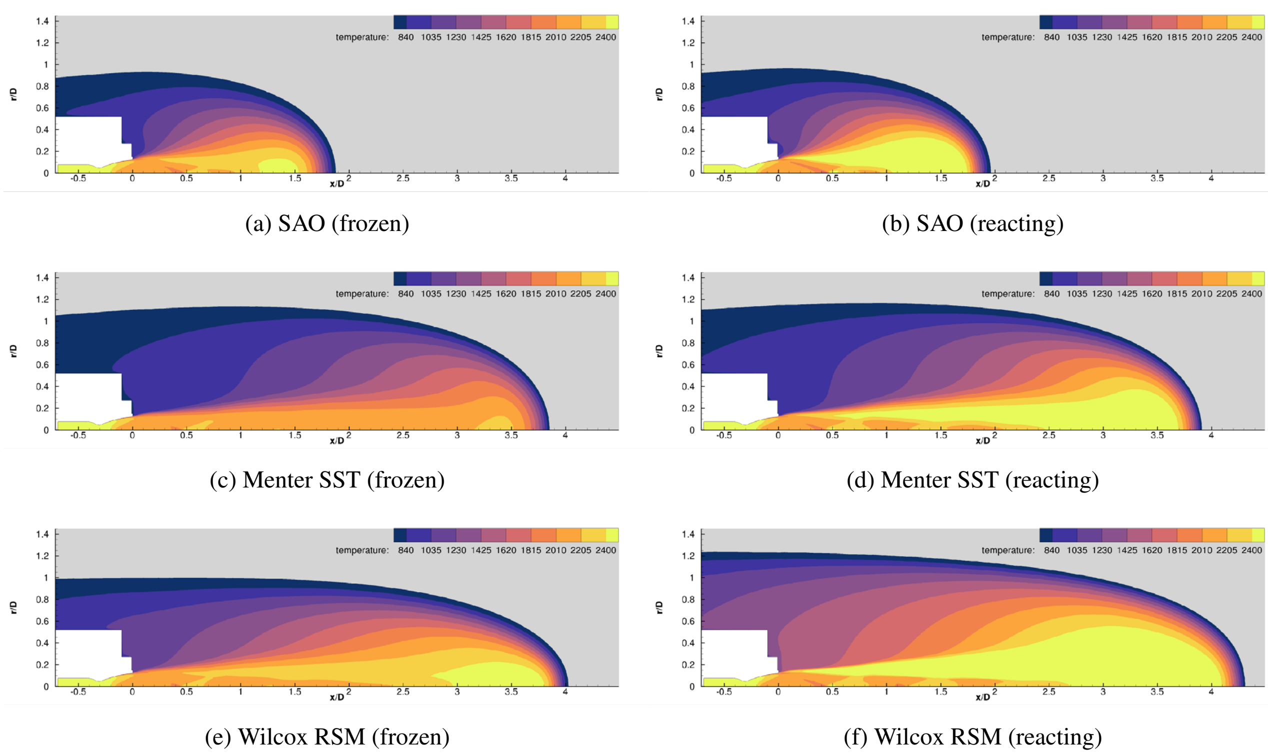

(a) SAO (frozen)

(b) SAO (reacting)

(c) Menter SST (frozen)

(d) Menter SST (reacting)

(e) Wilcox RSM (frozen)

(f) Wilcox RSM (reacting)

Fig. 6 Comparison of different chemical and thermodynamic models for the exhaust gas and and different turbulence models. Temperature scale in K. ($M = 0.84700$, $\rho = 0.94550$ kg/m^3

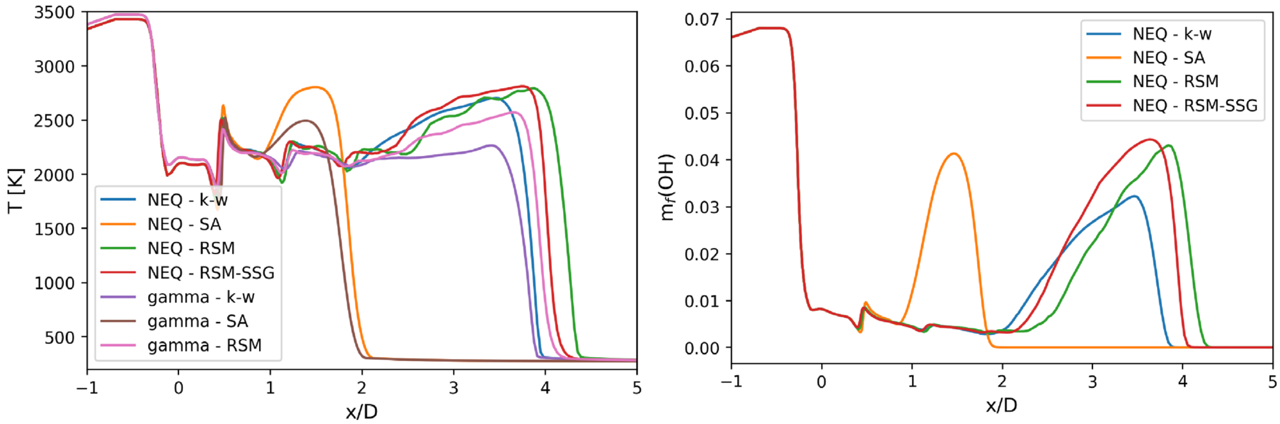

(a) plume centerline temperature

(b) plume centerline OH mass fraction

Fig. 7 Comparison of Spalart-Allmaras, Menter SST and RSM (Wilcox and SSG) turbulence model with full chemistry

database generation for phase *B* and phase *C*. The phase *B* database covers the CAL1B geometry and is used as a preliminary database during systems engineering. The generated database based on 2D and 3D CFD data is investigated with regards to integral loads, aeroshape dimensionality, the impact of dimensionality on local loads and the estimation of interpolation errors. Based on lessons learned, the database generation approach was adapted for the phase *C* database. The phase C database serves as the input for system requirements [28] and covers a much larger parameter space in terms of altitudes (density ρ given in kg/m^3), Mach numbers and angle of attack than the phase B database. Special cases like thrust vector deflection, thrust level and post-combustion chemistry are investigated separately to understand the aerothermal loads sensitives to parameters not considered in the database.

4.1 CFD solver settings and grids

For all calculations contained within the aerothermal database, the Spalart-Allmaras [44] (SA) one-equation eddy viscosity model in the original implementation without the trip term and the turbulence suppression term in laminar regions was used [44, 52]. This SA model is essentially a low-Reynolds-number model and requires a mesh with a properly resolved boundary-layer region (O(y+) ~1). An overview on the grid sizes for the different configurations is given in Table 5. Number of grid points vary from several hundreds of thousands for the 2D model to several million for the 3D models. A visualization of the grid on the symmetry plane and vehicle surface of the 3D models is shown in Fig. 8 for the CAL1B aeroshape. Grid refinement is applied to the near vehicle volumes and in the area of the plume. The nominal thermo-chemistry model for this study is based on a two species frozen gas model (frozen at nozzle exit) as described in Sect. 3.2. All heat flues are given in Terms of Nusselt number (Nu) based on aeroshell wall temperature and engine chamber temperature for reference temperature (compare table 2).

Table 5 Grid information

Aeroshape	Configuration	Number of grid points	Symmetry
Generic	UFO (2D)	3.6×10^5	1 degree 2D slice
CAL1B	UFO	5.6×10^6	Half symmetry 3D
CAL1B	UUO	9.1×10^6	Half symmetry 3D
CAL1C	UFO	23×10^6	Full 3D
CAL1C	UUO	23×10^6	Full 3D

4.2 Phase B aerothermal loads

Due to the large parameter space of the landing approach, the basis of the aerothermal database originates from 2D computations. Based on the different configurations the database is refined using more detailed high-fidelity 3D computations, especially at points where 3D flow effects play a major role. The two-dimensional calculations build the foundation for the database and allow it to cover a large and equal spaced parameter space in terms of density, Mach number and wall temperatures. A variation of generic trajectories depicting the landing approach show the crucial section of the flight corridor. More information on mission design and the approach and landing system can be found in Desmariaux et al. [11].

At the points close to the majority of sample trajectories calculations in 3D UFO configuration were performed. In the flight domain were both legs closed and legs open configurations are possible, both 3D UFO and 3D UUO

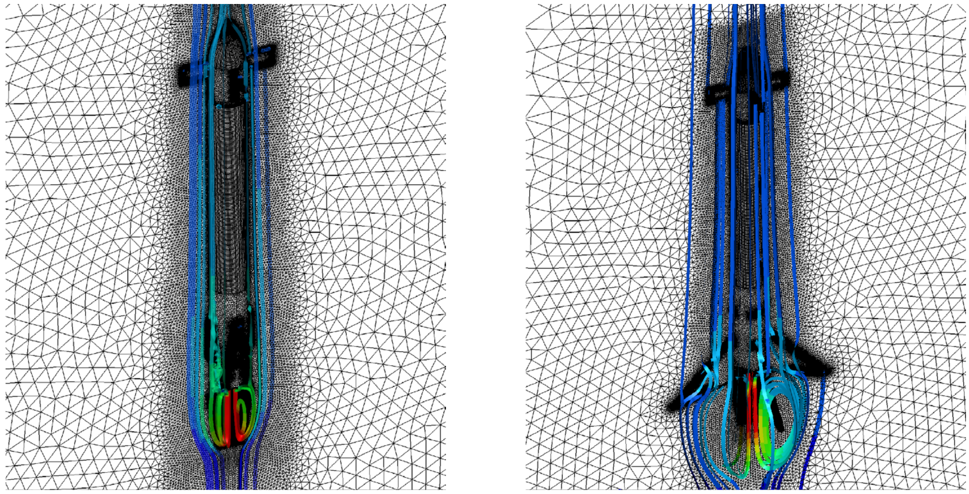

Fig. 8 Visualization of the grids used for CAL1B

(a) UFO configuration

(b) UUO configuration

configuration are considered for computations. The flight domain and calculation matrix chosen for the aerothermal load estimation for phase *B* is shown in Fig. 9. All colored trajectories marked within this figure are used in the same color scheme for the subsequent on-trajectory analyses. For the phase *B* database the 1976 standard atmosphere [53] was used. For the subsequent phase C database the CSG atmosphere data was applied.

4.2.1 Aerothermal database generation CAL1B aeroshape

The phase *B* aerothermal database is based on 75 2D CFD calculations and 13 high-fidelity 3D CFD calculations, all performed for 180 deg AoA.

The final database is assembled as follows:

1. 2D calculations are used as first support points for all conditions (density and Mach number and temperature). The average interface heat flux is calculated.
2. UFO 3D calculations are performed for selected trajectory points. The average interface heat flux is calculated and replaces selected 2D support points.
3. A second database is generated where UFO 3D points are replaced by UUO 3D points. This second database is used to evaluate conditions with open legs using linear interpolation.
4. Wall temperature influence on wall heat flux at the 3D conditions is estimated by applying the 2D gradient (dQ/dT) to the 3D condition.

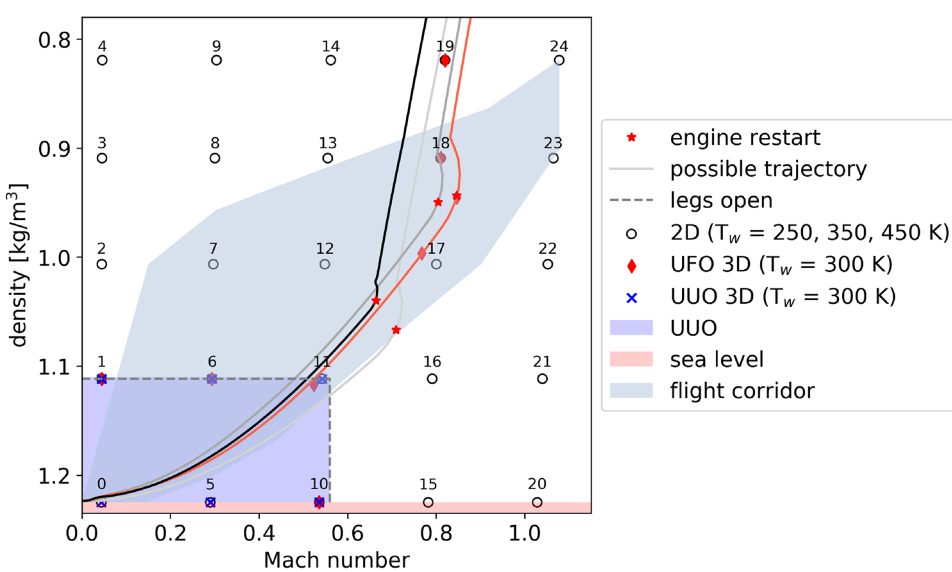

Fig. 9 Calculation matrix for phase B database. Based on 1976 standard atmosphere

The average heat flux at any given trajectory point (M, ρ, T_w) on each interface can then be found by evaluating the following relation:

$$Q(M, \rho, T_w) = \underbrace{Q(M_i, \rho_i, 180deg, 300K)}_{2D/3D} + (dQ/dT)_{2D}(300K - T_w) \tag{2}$$

4.2.2 Evaluation of integral loads and aerosphape dimensionality

The integral rate of heat flow at all database points is shown in Fig. 10. The area-averaged heat flux is largely dependent on relative Mach number and density. The convective heat flux scales with Mach number and density, and reaches the maximum values at high relative Mach numbers and densities. The sample trajectories indicate the main region of interest. The star markers mark the moment of engine retro boost start and are in the Mach number region of between 0.5 and 0.85 with integral rates of heat flow of up to 2.5 MW at the moment of engine ignition. Generally, it can be differentiated between trajectories with ignition at relatively low Mach numbers and high atmospheric density (low altitude) and ignition at higher Mach numbers and low densities-both scenarios lead to approximately the same order of magnitude of initial integral heat loads. The underlying trajectory design is related to a complex optimization process limited by thermal loads, structural loads, site regulations and demonstration flight objectives [11, 54] and will not be further discussed in this study.

To evaluate the database and the influence of the different 2D/3D configurations of the integral rate of heat flow and heat uptake along the different trajectories is estimated. The different configurations include a pure 2D configuration (2D), a 2D configuration supported by 3D UFO calculations (2D + UFO) and a 2D configuration supported by 3D UFO and UUO calculations, which includes the configuration change to landing legs (2D + UFO + UUO) at different flight times (-5 s and the earliest possible due to database inclusion).

For this comparison, the integral heat flow is the heat flux integrated over the area of the vehicle, while the heat uptake is the integral heat flow integrated over time-representing the heat uptake of the vehicle, assuming no losses due to radiation or wall temperature variation. The (area) integral rate of heat transfer and the total energy transfer into the vehicle is shown in Fig. 11a and b respectively. Two observations can be made: first, the maximum rate of heat flow varies significantly between trajectories, between 2 MW and 2.6 MW (for 2D database), secondly the difference between the purely 2D database and the 2D/3D database is rather small if the angle of attack is not taken into account. In terms of total heat energy transferred into the vehicle the range between possible trajectories is even larger with some trajectories presenting with almost double the total heat energy transferred into the vehicles than others.

4.2.3 Impact of dimensionality on average local loads

The aerothermal database contains the the average local on all considered aeroshape interfaces. These results are essential for the determination of the technical requirements passed on to product owners. In this section, the influence of dimensionality on representative interfaces, namely the fairing, legs, aft-bay and baseplate are evaluated. The average local loads expressed in average Nu number on these interfaces are shown in Fig. 12. In the figure results for a pure 2D database (2D), as well as a 3D supported database (2D + 3D UFO) are shown for selected trajectories. The filled circles indicate the max distance of the current flight condition to the next database support point. This distance is largest in the late stages of the return trajectory. For future databases, it was decided to refine the database especially close to the flown trajectories. For this database the angle of attack is not varied but fixed at 180 deg, therefore the differences between 2D and 3D are mainly geometric. For for interfaces close to the aft end and with dimensions close to 2D axisymmetric shape (e.g the baseplate) only minimal differences between 2D and 3D data is observed. The sections with larger distances

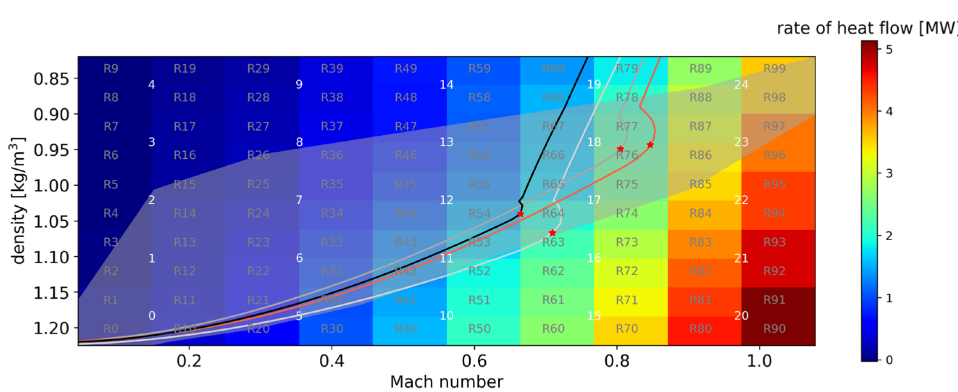

Fig. 10 Integral heat transfer rate on aft bay based on 2D results ($T_W = 300\ K$)

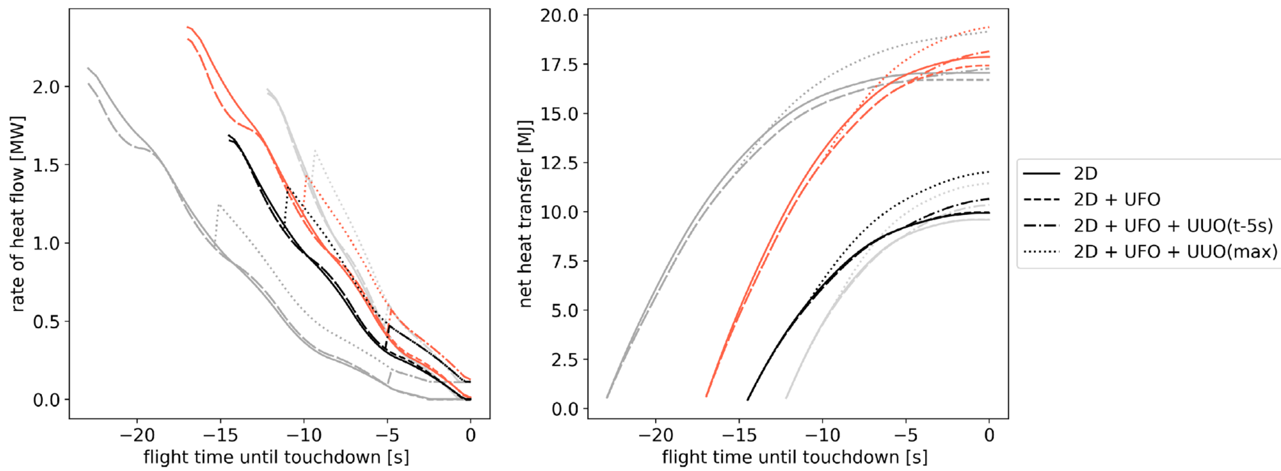

(a) integral heat transfer rate into vehicle

(b) integral heat energy transferred into vehicle

Fig. 11 Integral thermal loads assuming constant wall temperature (T_W = 300 K) for several different landing trajectories. Shown trajectories refer to trajectories shown in Fig. 9. Comparison for angle of attack of 180 deg

to the 3D data do not appear to be affected negatively. For the aft-bay the thermal loads in dimensional unites are between 60 and 30 kW/m^2 which is a factor of up to 5 higher than thermal loads during supersonic reentry calculated for the Falcon 9 [13] on the sidewall, as well as the base measured data on Ariane 5 [24] during ascent. This means special consideration with regard to TPS selection and refurbishment may be necessary.

4.2.4 Estimate of interpolation errors

The errors due to database point spacing/scarcity and interpolation are estimated by comparing the CAL1B interpolated database (based on 2D data only) heat flux with values obtained on points that are directly located on the representative trajectory (see Fig. 13). A comparison between the heat fluxes from the flight aerothermal database, its support points and the results from the landing aerothermal database for both the fairing and the baseplate are shown in Fig. 14. It can be seen that the relative errors at conditions of high heat flux are fairly small, approx. between 5 to 10% (Support points 1–3) but increase quickly as the average thermal load the vehicle encounters is dropping rapidly towards the end of the trajectory. Averaged over all interfaces the max absolute error in Nu number is between 25 and 100 for all support points (compare Fig. 15). For phase *C* the 2D and 3D data spacing was significantly reduced, which should lead to smaller interpolation errors. Further, the number of the 3D support points around the majority of considered trajectories was increased by a factor of 3.

4.2.5 Influence of angle of attack

The effect of the angle of attack was investigated at conditions close to database points 17 and 18 (compare Fig. 9). The overall total rate of heat flow as a function of the angle of attack is shown in Fig. 16 for the UFO configuration. Generally speaking the maximum rate of heat flow into the vehicle is highest at 180 deg angle of attack. However, looking at the spatial distribution, varying the angle of attack can have a significant impact on local heating.

The surface distribution of the heat flux for varying angles are shown in Fig. 17. At 180 deg angle of attack equal heating due to the plume-vehicle interaction is present. Changing the angle of attack to 175 deg increases the thermal loads on the aft bay, tanks and fin section due to plume impingement on the vehicle. At larger angles of attack the thermal loads are concentrated on the aft bay section as a majority of the plume is diverted into the free stream and does not interact with the vehicle. The averaged heat fluxes on the thermal interfaces are shown in Fig. 18, showing the same aforementioned trends. The influence of the angle of attack was not included in the aerothermal database but the results prompted to include this variable for the phase C database.

4.3 Phase C aerothermal loads

The flight domain and calculation matrix chosen for the aerothermal load estimation for phase C is shown in Fig. 19. The number of CFD computations for phase C is increased due to larger parameter space covering a larger envelope of return flight options. Additionally, the asymmetric cable and duct components on CAL1C aeroshape require full 3D

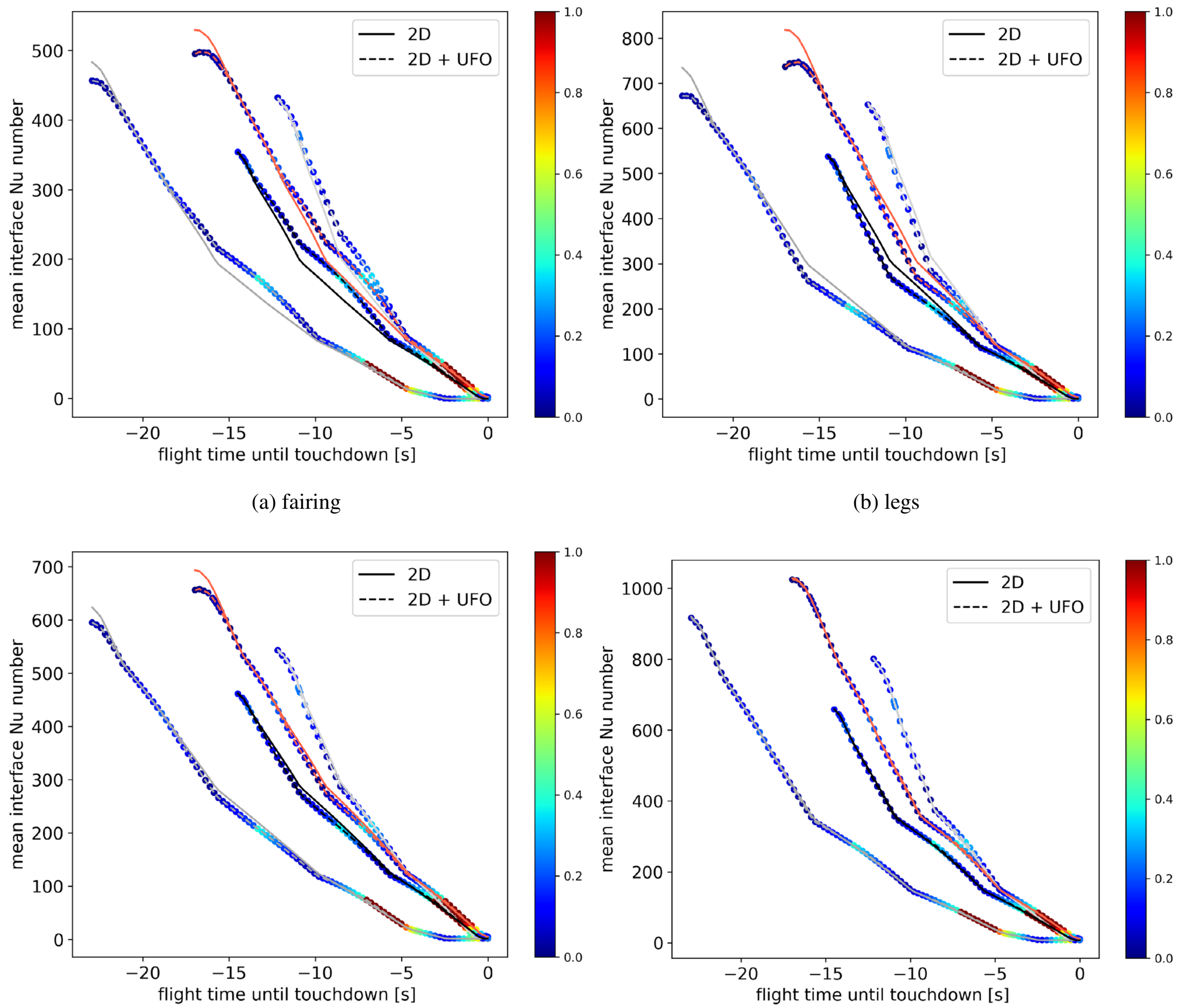

(a) fairing

(b) legs

(c) aft bay

(d) baseplate

Fig. 12 Comparison of local heat flux during representative trajectory ($T_W = 300\ K$). Lines indicate 2D database, dashed lines indicate 3D supported database, the filled circle indicates the maximum distance to database support point. Shown trajectories refer to trajectories shown in Fig. 9. Comparison for angle of attack of 180 deg

computations compared to phase B where half symmetry could be assumed. Further for CAL1B aerothermal data the 1976 Standard Atmosphere was used, while for CAL1C aerothermal data the Guiana Space Centre (CSG) atmosphere data relevant for the test and demo flights were used. This change resulted in an overall lower mean heatflux due to differences in ambient gas temperatures.

4.3.1 Database generation CAL1C aeroshape

The phase C aerothermal database is based on 153 2D CFD calculations and 30 high-fidelity 3D CFD calculations, all performed for 180 deg AoA. Additionally, multiple calculations both for UFO and UUO at different angles of attack were performed. The final database (compare Fig. 19) is assembled as follows:

1. 2D calculations are performed as support points for a wide range of conditions (density and Mach number and temperature). Each support point calculation is performed for 3 different wall temperatures.
2. 3D calculations are performed on a finer grid close to possible trajectory flight points at a wall temperature of 300 K.

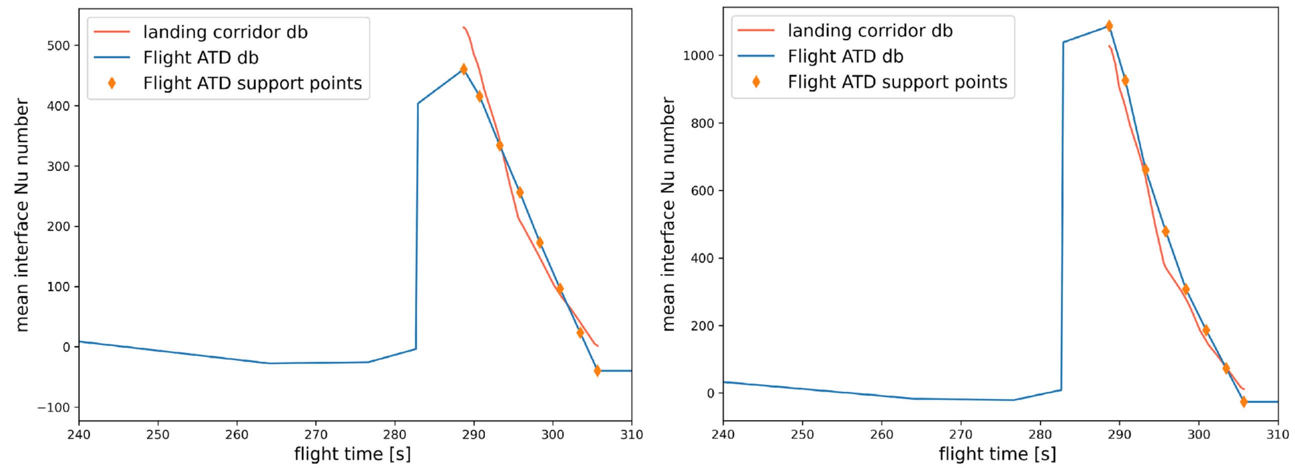

(a) fairing

(b) baseplate

Fig. 13 Comparison between interface heat flux predicted from the landing corridor database and flight aerothermal database (representative trajectory) ($T_W = 300\ K$)

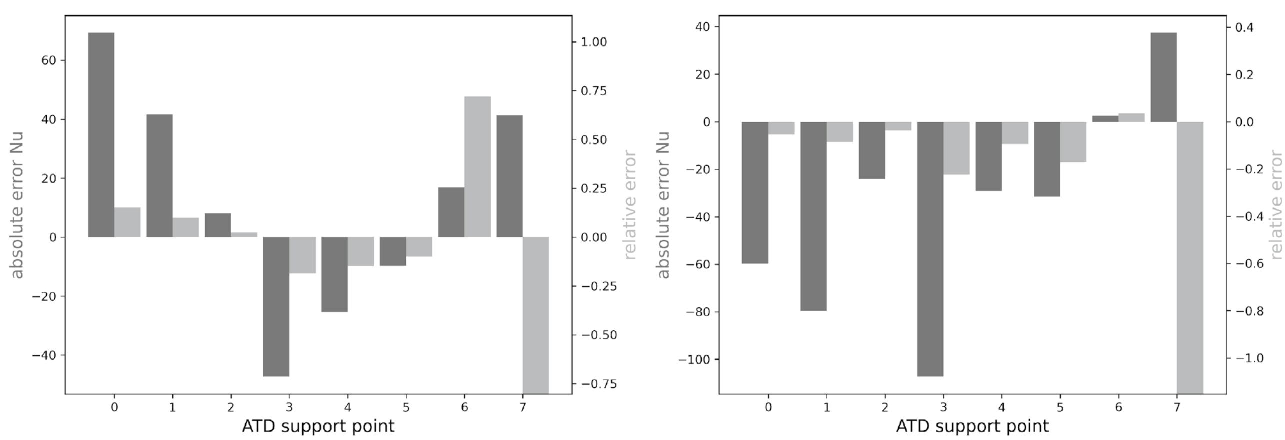

(a) fairing

(b) baseplate

Fig. 14 Absolute and relative errors on ATD points. ($T_W = 300\ K$)

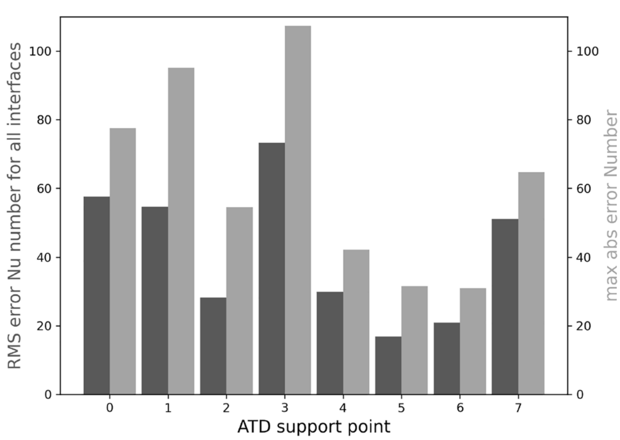

Fig. 15 RMS and max error on all interfaces ($T_W = 300\ K$)

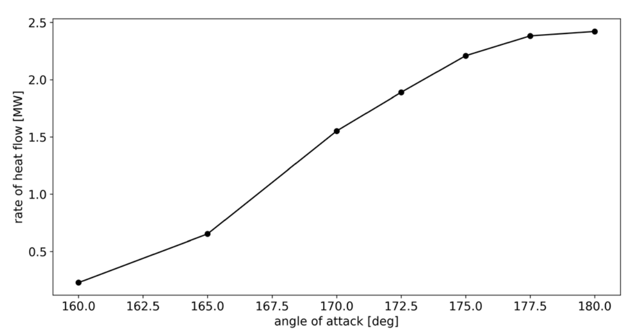

Fig. 16 Integral heat transfer rate on UFO configuration at varying angle of attack ($T_W = 300\ K$, $M = 0.8$)

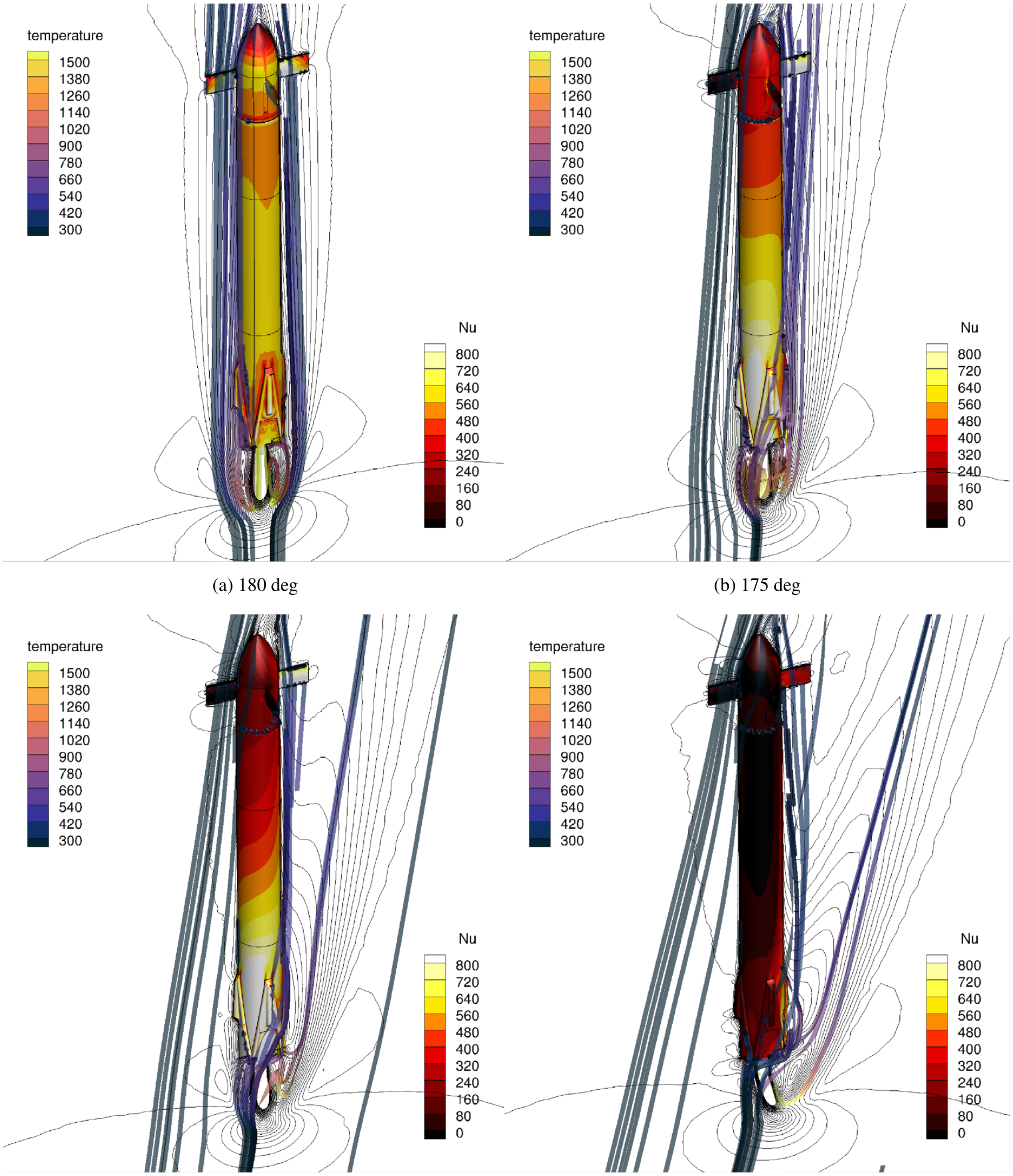

(a) 180 deg

(b) 175 deg

(c) 170 deg

(d) 165 deg

Fig. 17 Heat flux on UFO configuration at varying angle of attack (T_W = 300 K). Streamlines are colored by gas temperature in K, surface heat flux is given in terms of Nu number. Black lines indicate Mach number, but no scale is given

3. A study of selected AoA is performed for each 3D configuration at a single selected reference trajectory point at a wall temperature of 300 K.

The heat flux distribution at any given trajectory point (M, ρ, α, T_w) for each data point on each interface can then be found by evaluating the following relation:

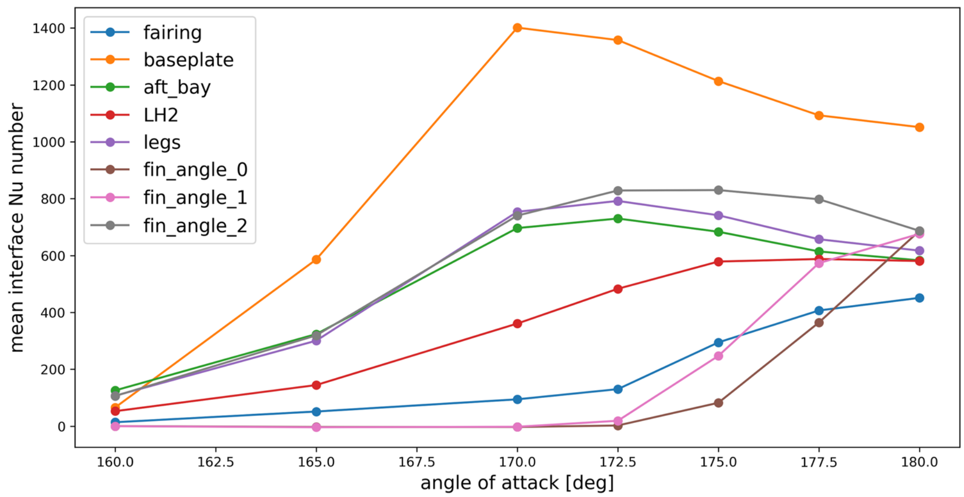

Fig. 18 Heat flux on UFO configuration at varying angle of attack ($T_W = 300\ K$, $M = 0.847$, $\rho = 0.9455 kg/m^3$)

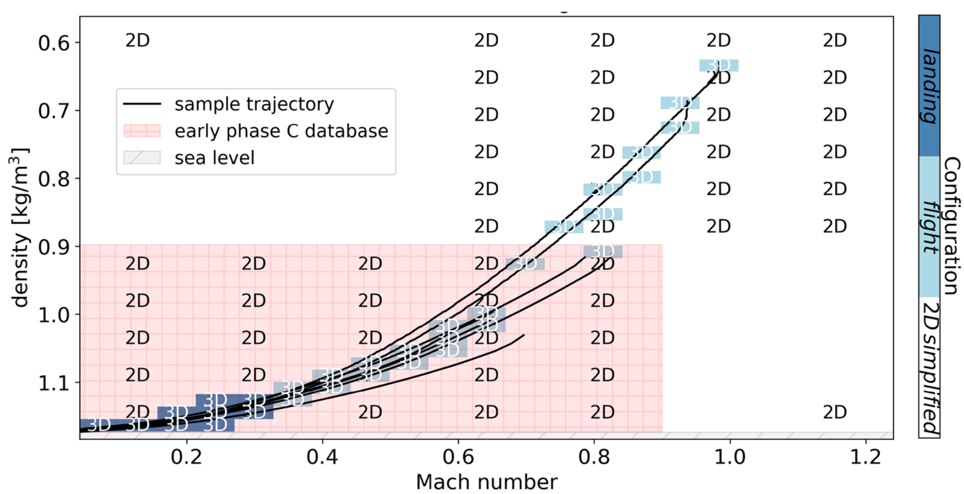

Fig. 19 Calculation matrix for the phase C databas. Freestream data is based on CSG atmosphere

$$Q(M, \rho, \alpha, T_w) = \left[\underbrace{Q(M_i, \rho_i, 180deg, 300K)}_{C1} + \underbrace{\Delta Q(AoA)}_{C2} \underbrace{\overline{Q_i(180deg)}}_{C3} \right] \underbrace{K}_{C4} + \underbrace{Q_{est}(T_w)}_{C5} \quad (3)$$

The single terms from left to right (C1–C5) are:

The 3D data at the closest trajectory point to the chosen evaluation point (M, ρ, α, T_w):

$$Q(M_i, \rho_i, 180deg, 300K) \quad (C1)$$

where the subscript i refers to the nearest 3D data point.

The AoA dependency is based on the difference between the heat flux at 180 deg AoA and the selected angle, normalized by the mean interface heatflux at this trajectory point:

$$\Delta Q(AoA) = \Delta Q(M_a, \rho_a, \alpha, 300K) / \overline{Q(M_a, \rho_a, 180deg, 300K)} \quad (C2)$$

where

$$\Delta Q(M_a, \rho_a, \alpha, 300K) = Q(M_a, \rho_a, \alpha, 300K) - Q(M_a, \rho_a, 180deg, 300K) \quad (4)$$

and the subscript a refers to AoA data at a reference UFO/UUO trajectory point and the mean interface heat flux is defined as follows:

$$\overline{Q_i(180deg)} = \overline{Q(M_i, \rho_i, 180deg, 300K)} \quad (C3)$$

To account for the wide range of conditions the data is scaled based on the 2D data with a scaling factor. This scaling factor is the ratio of the mean interface heat flux of the evaluated interpolated trajectory point to mean interface heat flux of the nearest (3D data) trajectory point:

$$K = \overline{Q_{2D}(M, \rho, 180deg, 300K)} / \overline{Q_{2D}(M_i, \rho_i, 180deg, 300K)} \tag{C4}$$

Finally, the wall temperature influence on wall heat flux is estimated by applying the interpolated 2D gradient (dQ/dT), which is based on three wall temperatures to the chosen evaluation point 3D conditions:

$$Q_{est}(T_w) = (dQ/dT)_{2D}(300K - T_w) \tag{C5}$$

For systems engineering purposes the heat flux distribution is averaged for each interface and saved to a database file. This database creation method was choosen as it is very robust and should minimize additional uncertainties due to interpolation artifacts.

4.3.2 Local loads during flight

The local loads on selected interfaces are shown in Fig. 20 for both CAL1B and CAL1C databases. While for CAL1B aerothermal data the 1976 Standard Atmosphere was used, CAL1C aerothermal data assumes Guiana Space Centre (CSG) atmosphere data relevant for the test and demo flights. The change in atmosphere profile was also applied to the relevant trajectory data. This change resulted in a generally overall lower mean heatflux due to differences in ambient gas temperatures. However, due to higher ground ambient temperatures higher loads are seen right before touchdown.

4.3.3 Special cases

Special cases not covered in the aerothermal database are shown for the UFO configuration in the following figures

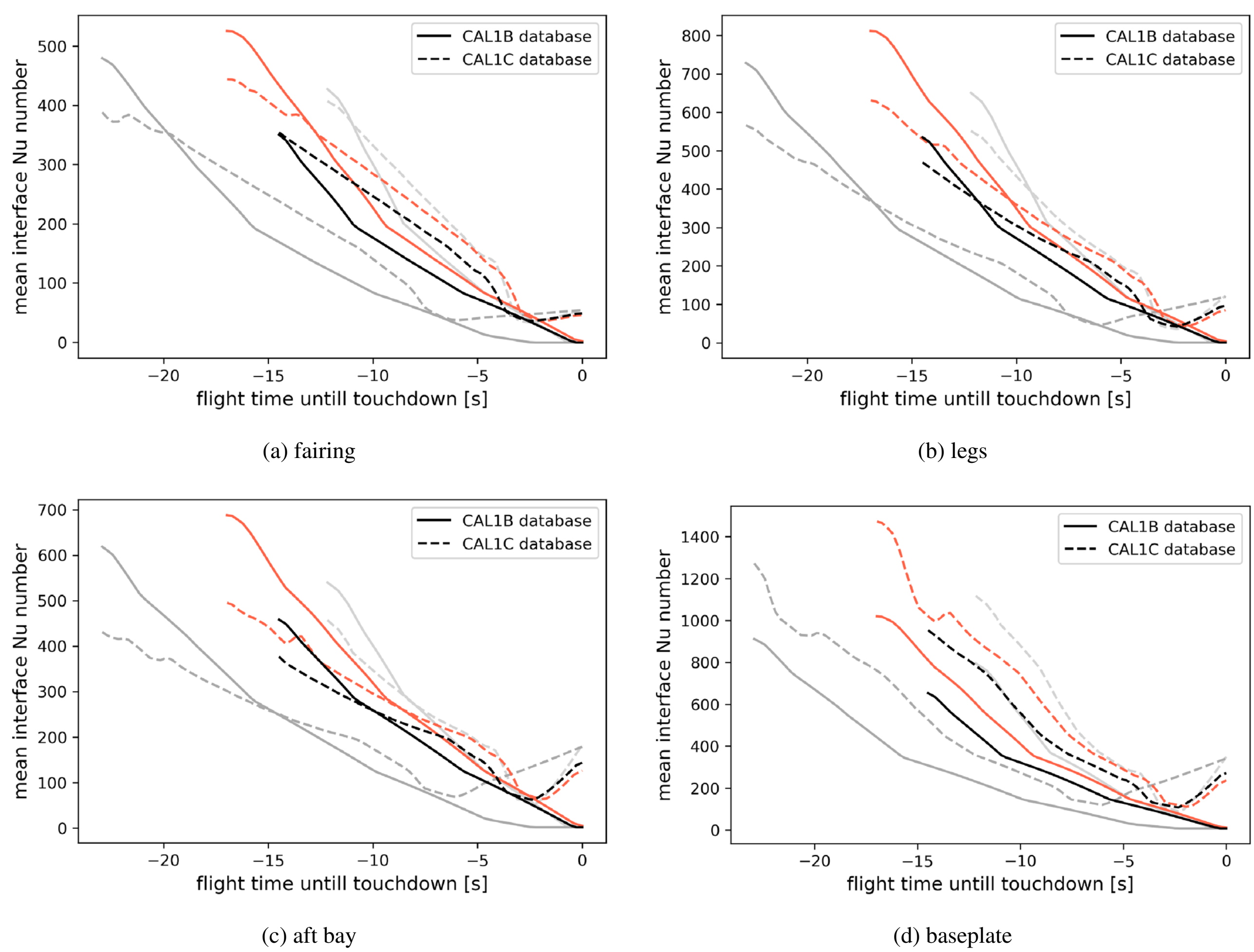

(a) fairing

(b) legs

(c) aft bay

(d) baseplate

Fig. 20 Comparison of CAL1B database and CAL1C database for selected trajectories (UFO configuration). Shown trajectories and their line colors refer to trajectories shown in Fig. 9

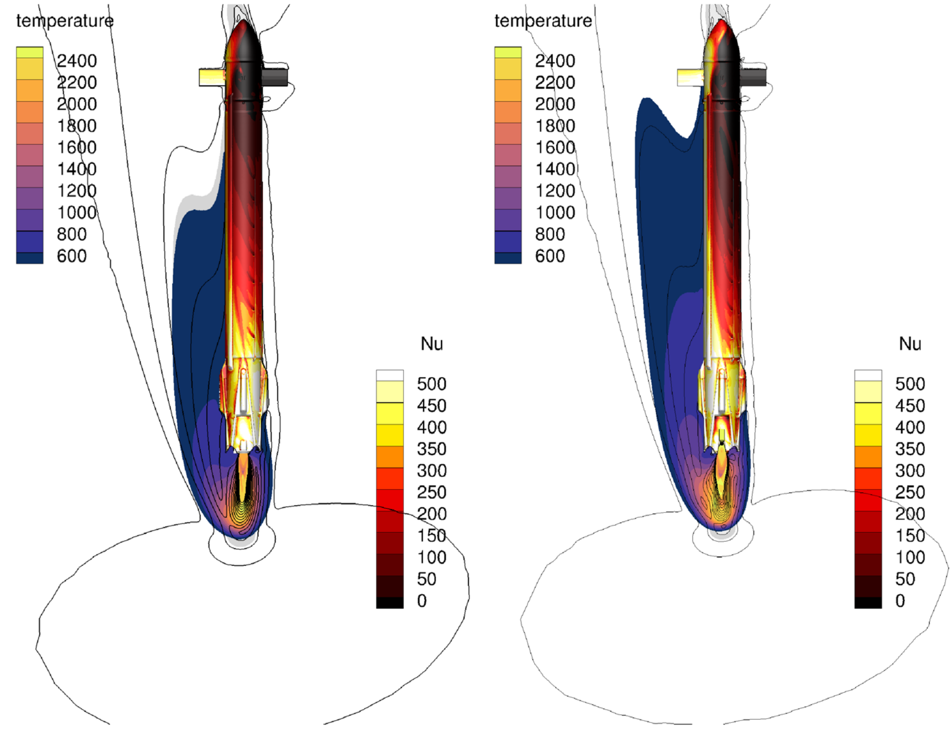

(a) 170 deg (nominal) (b) 170 deg (chemical)

Fig. 21 Heat flux on UFO configuration for nominal and chemically reactive plume ($T_W = 300\ K$, $M = 0.8$, $\rho = 0.72065 kg/m^3$). Field contours are colored by gas temperature in K, surface heat flux is given in terms of Nu number. Black lines indicate Mach number, but no scale is given

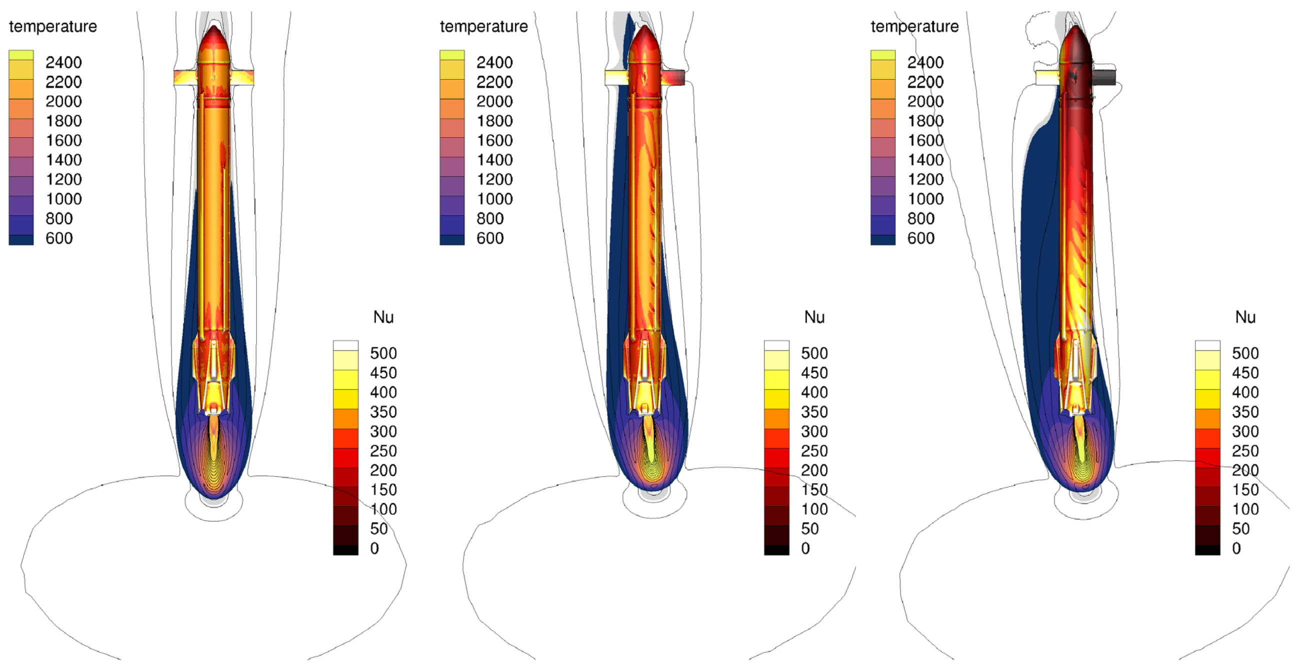

(a) 180 deg (nominal) (b) 175 deg (5 deg TVC) (c) 170 deg (5 deg TVC)

Fig. 22 Heat flux on UFO configuration for nominal and TVC deflection ($T_W = 300$ K, $\underline{M} = 0.8$, $\rho = 0.72065 kg/m^3$). Field contours are colored by gas temperature in K, surface heat flux is given in terms of Nu number. Black lines indicate Mach number, but no scale is given for the impact of chemistry, thrust vector control and throttle level.

For 170 deg angle of attack the influence of post combustion chemistry is visualized in Fig. 21. While the load distribution is similar, differences in local loads, slightly lower loads on the aft bay region and slightly higher loads on the fin and fairing can be observed at these flight conditions. Similar to the 2D preparatory studies presented in the beginning slightly higher gas temperatures are present within the core and past the aft. This results in the higher thermal loads sensed by the downstream interfaces.

The effect of thrust vector deflection (5 deg thrust vector) on the thermal loads and the plume deflection are compared to reference conditions in Fig. 22. While there a local changes present, leading to higher thermal loads towards the general load cases are roughly comparable to a case without TVC adjusted for the effective wind angle (similar to adjustment in aerodynamic forces [26]). Further analysis is required to quantify the added uncertainty from using such an approximation.

The RSR engine supplied by JAXA/MHI is restartable and throttable between 21 and 109% thrust. The effect of engine throttling is visualized in Fig. 23 for levels between 20% and 110% compared to nominal. Reducing engine thrust, respectively reducing engine mass flow rate leads to a direct reduction in heat fluxes on all interfaces. The database only uses data with a nominal thrust level, therefore a conservative treatment of this effect is ensured in the database. Reducing the engine thrust levels to idle mode can lead to nozzle unchoking and is therefore not consider, however, no significant thermal loads are expected.

5 Summary

Aerothermal loads are a design driving factor during launcher development as the thermal loads directly influence thermal protection system design and trajectory. For the purpose of characterizing the aerothermal properties and loads of the CALLISTO vehicle during the design cycle, aerothermal databases are generated periodically based on the current aeroshape and flight domain. In this study the CALLISTO general flight profile, vehicle configuration, and the relevant thermal interfaces are described for both phase *B* (CAL1B) and *C* (CAL1C) aeroshapes. Additionally the flight domain which defines the numerical effort is minutely detailed. Due to the large parameter space of the landing approach, the basis of the aerothermal database originates from 2D computations and is refined using more detailed high fidelity 3D computations near the critical trajectory points. The database development for vehicle phase *B* and phase *C* are described and analysed for some of the most prominent interfaces. Due to the collaborative nature of the

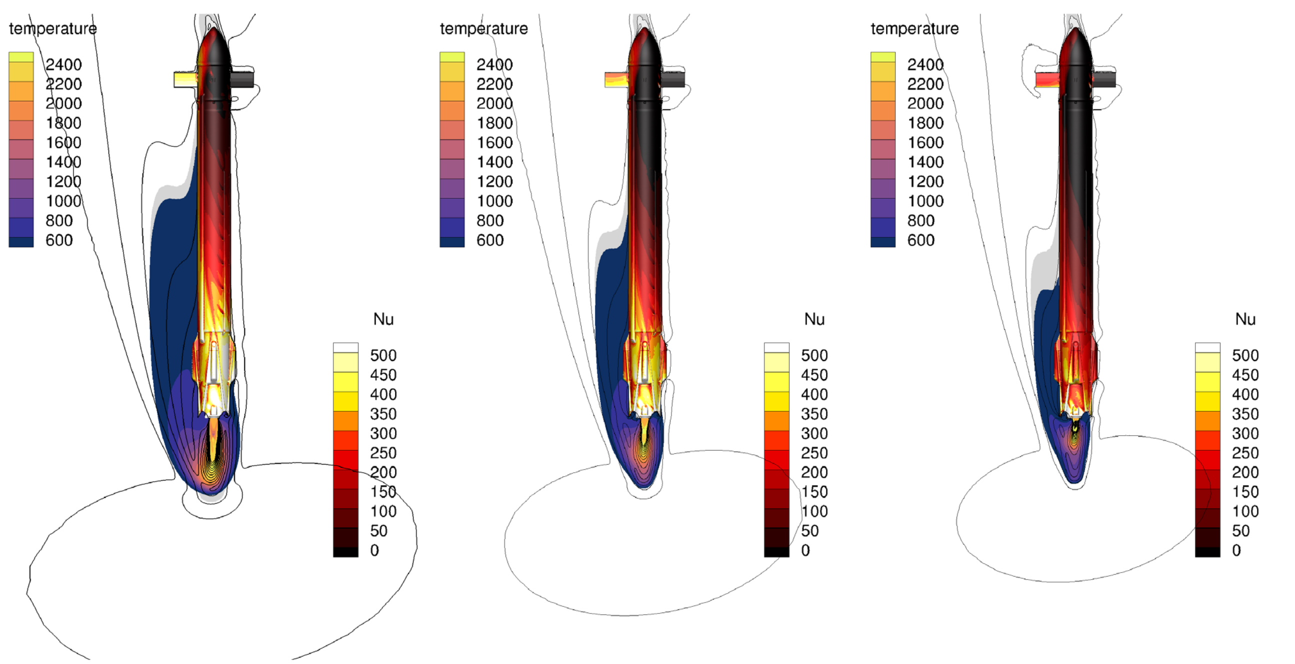

(a) 170 deg (110% thrust) (b) 170 deg (40% thrust) (c) 170 deg (20% thrust)

Fig. 23 Heat flux on UFO configuration for varying thrust level (T_W = 300 K, M = 0.8, $\rho = 0.72065 kg/m^3$). Field contours are colored by gas temperature in K, surface heat flux is given in terms of Nu number. Black lines indicate Mach number, but no scale is given

CALLISTO design process loads definition and respective thermal interfaces (tanks, legs, etc.) for the entire vehicle are defined. While the CAL1B aeroshape had 15 thermal interfaces, the number of interfaces for the CAL1C aeroshape had more than 50 thermal interfaces due to its detailed description involving no symmetry and many of the final mechanical extensions (cable ducts, pipes, etc.). While the phase B aerothermal database is based on 75 2D CFD calculations and 13 high fidelity 3D CFD calculations, the extend of the phase *C* aerothermal database was tripled to 153 2D CFD calculations and more than 40 high fidelity 3D CFD while the number of grid points increased equally. Studies of the phase *B* database showed that for interfaces close to the aft end and with dimensions close to 2D axisymmetric shape (e.g the baseplate) only minimal differences between 2D and 3D data is observed near 180 deg AoA. Interpolation errors for a coarse trajectory were estimated to be approx. between 5 to 10% (support points 1–3) at trajectory points with high thermal loads but also increase quickly as the average thermal load the vehicle encounters is dropping rapidly towards the end of the trajectory. At high subsonic speeds, the maximum thermal loads are up to 5 times higher in average than found for configurations like the expendable Ariane 5 during ascent or the reusable Falcon 9 during supersonic reentry. Finding that the angle of attack can have a significant impact on the local heating during a phase *B* study prompted to include this parameter as an independent variable for the phase *C* database. The final phase *C* database presented allows interpolation of interface heatfluxes for the entire flight domain at a varying angle of attack (between 180 deg and 160 deg). Further, the sensitivity of the plume-vehicle interaction to angle of attack, chemistry, thrust vector deflection and engine throttling are investigated for a critical Mach number (close to max. Mach number for engine restart) indicating further area of improvement for future databases.

Appendix

See Table 6.

Table 6 Gerlinger reaction mechanism

No	Reaction			Rate constants		
				A	n	E_a
1	$H_2 + O_2$	$\rightleftharpoons$	$HO_2 + H$	1.0000e+14	0.00	5.6000e+04
2	$H + O_2$	$\rightleftharpoons$	$HO + O$	2.6000e+14	0.00	1.6800e+04
3	$O + H_2$	$\rightleftharpoons$	$HO + H$	1.8000e+10	1.00	8.9000e+03
4	$HO + H_2$	$\rightleftharpoons$	$H_2O + H$	2.2000e+13	0.00	5.1500e+03
5	$2\,HO$	$\rightleftharpoons$	$H_2O + O$	6.3000e+12	0.00	1.0900e+03
6[a]	$H + HO + M$	$\rightleftharpoons$	$H_2O + M$	2.2000e+22	−2.00	0.0000e+00
7[b]	$2\,H + M$	$\rightleftharpoons$	$H_2 + M$	6.4000e+17	−1.00	0.0000e+00
8[c]	$H + O + M$	$\rightleftharpoons$	$HO + M$	6.0000e+16	−0.60	0.0000e+00
9[d]	$H + O_2 + M$	$\rightleftharpoons$	$HO_2 + M$	2.1000e+15	0.00	−1.0000e+03
10	$HO_2 + H$	$\rightleftharpoons$	$2\,HO$	1.4000e+14	0.00	1.0800e+03
11	$HO_2 + H$	$\rightleftharpoons$	$H_2O + O$	1.0000e+13	0.00	1.0800e+03
12	$HO_2 + O$	$\rightleftharpoons$	$O_2 + HO$	1.5000e+13	0.00	9.5000e+02
13	$HO_2 + HO$	$\rightleftharpoons$	$H_2O + O_2$	8.0000e+12	0.00	0.0000e+00
14	$2\,HO_2$	$\rightleftharpoons$	$H_2O_2 + O_2$	2.0000e+12	0.00	0.0000e+00
15	$H + H_2O_2$	$\rightleftharpoons$	$H_2 + HO_2$	1.4000e+12	0.00	3.6000e+03
16	$O + H_2O_2$	$\rightleftharpoons$	$HO + HO_2$	1.4000e+13	0.00	6.4000e+03
17	$HO + H_2O_2$	$\rightleftharpoons$	$H_2O + HO_2$	6.1000e+12	0.00	1.4300e+03
18[e]	$H_2O_2 + M$	$\rightleftharpoons$	$2\,HO + M$	1.2000e+17	0.00	4.5500e+04
19	$2\,O + M$	$\rightleftharpoons$	$O_2 + M$	6.0000e+13	0.00	−1.8000e+03

Units in cm, mol, cal, s

[a] $H_2O = 6.0$

[b] $H_2 = 2.0, H_2O = 6.0$ [c] $H_2O = 5.0$

[d] $H_2 = 2.0, H_2O = 16.0$

[e] $H_2O = 15.0$

Acknowledgements The authors gratefully acknowledge the scientific support and HPC resources provided by the German Aerospace Center (DLR). The HPC system CARO is partially funded by "Ministry of Science and Culture of Lower Saxony" and "Federal Ministry for Economic Affairs and Climate Action".

Author Contributions T. E. wrote the main manuscript text and J. K. prepared some of the figures .All authors contributed to the discussion. All authors reviewed the manuscript.

Funding Open Access funding enabled and organized by Projekt DEAL.

Declarations

Conflict of interest The authors declare no competing interests.

References

1. Reijasse, P., Delery, J.: Investigation of the flow past the ariane 5 launcher afterbody. J. Sp. Rock. **31**(2), 208–214 (1994). https://doi.org/10.2514/3.26424
2. Kramer, O.: Evaluation of thermal radiation from the Titan III solid rocket motor exhaust plumes, (1970). https://doi.org/10.2514/6.1970-842
3. Greenwood, T.F., Lee, Y.C., Bender, R.L., Carter, R.E.: Space shuttle base heating. J. Sp. Rock. **21**(4), 339–345 (1984). https://doi.org/10.2514/3.25660
4. Vila, J., Hassin, J.: Technology acceleration process for the themis low cost and reusable prototype. In: 8th European Conference for Aeronautics and Space Sciences (EUCASS), Madrid (2019). https://doi.org/10.13009/EUCASS2019-97
5. Préaud, J.-P., Dussy, S., Breteau, J.B., Bru, J.B.: Preparing the future of european space transportation: reusable technologies and demonstrators. In: 8th European Conference for Aeronautics and Space Sciences (EUCASS), Madrid (2019). https://doi.org/10.13009/EUCASS2019-973
6. Iannetti, A., Girard, N., Ravier, N., Edeline, E., Tchou-Kien, D.: PROMETHEUS, a low cost LOX/CH4 engine prototype. https://doi.org/10.2514/6.2017-4750
7. de Patureau Mirand, A., Bahu, J.-M., Gogdet, O.: Ariane next, a vision for the next generation of ariane launchers. Acta. Astronaut **170**, 735–749 (2020). https://doi.org/10.1016/j.actaastro.2020.02.003
8. Dumont, E., Ishimoto, S., Tatiossian, P., Klevanski, J., Reimann, B., Ecker, T., Witte, L., Riehmer, J., Sagliano, M., Vincenzino, S.G., Petkov, I., Rotärmel, W., Schwarz, R., Seelbinder, D., Markgraf, M., Sommer, J., Pfau, D., Martens, H.: Callisto: a demonstrator for reusable launcher key technologies. Trans. JSASS Aerospace Tech. Japan **19**(1), 106–115 (2021). https://doi.org/10.2322/tastj.19.106
9. Dumont, E., Ishimoto, S., Illig, M., Sagliano, M., Solari, M., Ecker, T., Martens, H., Krummen, S., Desmariaux, J., Saito, Y., Ertl, M., Klevanski, J., Reimann, B., Woicke, S., Schwarz, R., Seelbinder, D., Markgraf, M., Riehmer, J., Braun, B., Aicher, M.: Callisto: towards reusability of a rocket stage: current status. In: 33rd ISTS Conference (2022). https://elib.dlr.de/185543/
10. Krummen, S., Desmariaux, J., Saito, Y., Boldt, M., Briese, L.E., Cesco, N., Chavagnac, C., CLIQUET-MORENO, E., Dumont, E., Ecker, T., Eichel, S., Ertl, M., Giagkozoglou, S., Glaser, T., Grimm, C., Illig, M., Ishimoto, S., Klevanski, J., Lidon, N., Mierheim, O., Niccolai, J.-F., Reershemius, S., Reimann, B., Riehmer, J., Sagliano, M., Scheufler, H., Schneider, A., Schröder, S., Schwarz, R., Seelbinder, D., Stief, M., Windelberg, J., Woicke, S.: Towards a reusable first stage demonstrator: callisto-technical progresses and challenges. In: Proceedings of the International Astronautical Congress, IAC (2021). IAC-21-D2.6.1. https://elib.dlr.de/147143/
11. Desmariaux, J., Cliquet-Moreno, E., Chavagnac, C., Dumont, E., Saito, Y.: Callisto: Its flight envelope and vehicle design. In: 8th European Conference for Aeronautics and Space Sciences (EUCASS), Madrid, Spain (2019). https://elib.dlr.de/133317/
12. ArianeGroup: arianegGoup selected for two european commission calls for projects to speed up the development of europe's first reusable and eco-friendly launchers. https://www.ariane.group/en/news/arianegroup-selected-for-two-european-commission-calls-for-projects-to-speed-up-the-development-of-europes-first-reusable-and-eco-friendly-launchers/ Accessed 2024
13. Ecker, T., Karl, S., Dumont, E., Stappert, S., Krause, D.: Numerical study on the thermal loads during a supersonic rocket retropropulsion maneuver. J. Sp. Rock **57**(1), 131–146 (2020). https://doi.org/10.2514/1.A34486
14. Ecker, T., Zilker, F., Dumont, E., Karl, S., Hannemann, K.: Aerothermal analysis of reusable launcher systems during retro-propulsion reentry and landing. In: Space Propulsion Conference 2018 (2018). https://elib.dlr.de/120072/
15. Dumont, E., Stappert, S., Ecker, T., Wilken, J., Karl, S., Krummen, S., Sippel, M.: Evaluation of future ariane reusable vtol booster stages. In: 68th International Astronautical Congress (2017). IAC-17-D2.4.3. https://elib.dlr.de/114430/
16. Dumont, E., Ecker, T., Chavagnac, C., Witte, L., Windelberg, J., Klevanski, J., Giagkozoglou, S.: Callisto - reusable vtvl launcher first stage demonstrator. In: Space Spropulsion Conference 2018 (2018). https://elib.dlr.de/119728/
17. Laureti, M., Karl, S., Bykerk, T., Kirchheck, D.: Aerothermal analysis of the retpro flight configuration. In: 3AF (ed.) 9th Edition of the 3AF International Conference on Space Propulsion 2024, pp. 1–11 (2024). https://elib.dlr.de/198838/
18. Bykerk, T.: A standard model for the investigation of aerodynamic and aerothermal loads on a re-usable launch vehicle. In: EUCASS, CEAS (eds.) 10th EUCASS - 9th CEAS 2023, pp. 1–12 (2023). https://elib.dlr.de/194475/
19. Marwege, A., Gülhan, A., Klevanski, J., Hantz, C., Karl, S., Laureti, M., De Zaiacomo, G., Vos, J., Jevons, M., Thies, C., et al.: Retalt: review of technologies and overview of design changes. Ceas Space J. **14**(3), 433–445 (2022). https://doi.org/10.1007/s12567-022-00458-9
20. Ertl, M., Ecker, T., Klevanski, J., Krummen, S., Dumont, E.: Aerothermal analysis of plume interaction with deployed landing legs of the callisto vehicle. In: 9th European Conference for Aeronautics and Space Sciences (2022). https://doi.org/10.13009/EUCASS2022-4686
21. Ertl, M., Ecker, T.: Aerodynamic and aerothermal comparison between the cal1c and cal1d geometries for the callisto vehicle. In: EUCASS, CEAS (eds.) 10th EUCASS - 9th CEAS 2023, pp.

1–12 (2023). https://doi.org/10.13009/EUCASS2023-431. https://elib.dlr.de/193847/
22. Laureti, M., Karl, S.: Aerothermal databases and load predictions for retro propulsion-assisted launch vehicles (retalt). CEAS Sp. J. (2022). https://doi.org/10.1007/s12567-021-00413-0
23. Klevanski, J., Ecker, T., Riehmer, J., Reimann, B., Dumont, E., Chavagnac, C.: Aerodynamic studies in preparation for callisto-reusable vtvl launcher first stage demonstrator. In: 69th International Astronautical Congress (IAC) (2018). IAC-18- D2.6.3. https://elib.dlr.de/122062/
24. Muylaert, J., Kordulla, W., Giordano, D., Marraffa, L., Schwane, R., Spel, M., Walpot, L., Wong, H.: Aerothermodynamic analysis of space-vehicle phenomena. ESA Bull. **2001**, 69–79 (2001)
25. Sivignon, T., Caillaud, J., Desmariaux, J.: Control law design for the callisto demonstrator. In: 8th European Conference for Aeronautics and Space Sciences (EUCASS), Madrid (2019). https://doi.org/10.13009/EUCASS2019-216
26. Klevanski, J., Reimann, B., Krummen, S., Ertl, M., Ecker, T., Riehmer, J., Dumont, E.: Progress in aerodynamic studies for callisto-reusable vtvl launcher first stage demonstrator. In: 9th European Conference for Aeronautics and Space Sciences (EUCASS) (2022). https://elib.dlr.de/187069/
27. Vincenzino, S.G., Eichel, S., Rotärmel, W., Krziwanie, F., Petkov, I., Dumont, E., Schneider, A., Schröder, S., Windelberg, J., Ecker, T., Ertl, M.: Development of reusable structures and mechanisms for callisto. In: 33rd ISTS Conference (2022). https://elib.dlr.de/185598/
28. Cliquet Moreno, E., Mauriès, A., Desmariaux, J., Krummen, S., Saito, Y., Biran, D.: Practical solutions for efficient & structured collaborative work in the frame of callisto, reusable launcher first stage international demonstrator. In: 9th European Conference For Aeronautics And Space Science, EUCASS 2022 (2022). https://elib.dlr.de/187030/
29. Giagkozoglou, S., Eichel, S., Rotärmel, W., Krziwanie, F., Petkov, I., Dumont, E., Schneider, A., Schröder, S., Windelberg, J., Ecker, T., Ertl, M.: Development of reusable structures and mechanisms for callisto. J. Evol. Sp. Act. (2023). https://doi.org/10.57350/jesa.36
30. Langer, S., Schwöppe, A., Kroll, N.: The DLR Flow Solver TAU–Status and Recent Algorithmic Developments. AIAA Paper AIAA-2014-0080 (2014) https://doi.org/10.2514/6.2014-0080
31. Schwamborn, D., Gerhold, T., Heinrich, R.: The dlr tau-code: recent applications in research and industry. In: ECCOMAS CFD 2006: Proceedings of the European Conference on Computational Fluid Dynamics, Egmond Aan Zee, The Netherlands, September 5-8, 2006 (2006). Delft University of Technology; European Community on Computational Methods
32. Schwamborn, D., Gerhold, T., Hannemann, V.: In: Nitsche, W., Heinemann, H.-J., Hilbig, R. (eds.) On the Validation of the DLR-TAU Code, pp. 426–433. Vieweg+Teubner Verlag, Wiesbaden (1999). https://doi.org/10.1007/978-3-663-10901-3_55
33. Cambier, L., Kroll, N.: Miracle-a joint dlr/onera effort on harmonization and development of industrial and research aerodynamic computational environment. Aerosp. Sci. Technol. **12**(7), 555–566 (2008). https://doi.org/10.1016/j.ast.2008.01.007
34. Knopp, T.: Validation of the turbulence models in the DLR TAU Code for transonic flows. A best practice guide (2006)
35. Mack, A., Hannemann, V.: Validation of the Unstructured DLR-TAU-Code for Hypersonic Flows. https://doi.org/10.2514/6.2002-3111
36. Wada, Y., Liou, M.-S.: An accurate and robust flux splitting scheme for shock and contact discontinuities. SIAM J. Sci. Comput. **18**(3), 633–657 (1997). https://doi.org/10.1137/S1064827595287626
37. van Leer, B.: Towards the ultimate conservative difference scheme. v. a second-order sequel to godunov's method. J. Comput. Phys. **32**(1), 101–136 (1979). https://doi.org/10.1016/0021-9991(79)90145-1
38. Horchler, T., Fechter, S., Hannemann, K.: Validation of the dlr tau code for scale-resolving combustion simulations. In: Space Propulsion 2018 (2018). https://elib.dlr.de/119337/
39. Hannemann, V.: Numerical simulation of shock-shock-interactions considering chemical and thermal nonequilibrium. In: DLR-Forschungsbericht 97-07 (1997)
40. Sato, M., Hashimoto, T., Takada, S., Kimura, T., Onodera, T., Naruo, Y., Yagishita, T., Niu, K.-I., Kaneko, T., Obase, K.: Development of main propulsion system for reusable sounding rocket: design considerations and technology demonstration. Trans. Jpn. Soc. Aeronaut. Sp. Sci. Aerosp. Technol. Jpn. **12**(ists29), 1–6 (2014). https://doi.org/10.2322/tastj.12.Tm_1
41. Kimura, T., Hashimoto, T., Sato, M., Takada, S., Moriya, S.-I., Yagishita, T., Naruo, Y., Ogawa, H., Ito, T., Obase, K., Ohmura, H.: Reusable rocket engine: firing tests and lifetime analysis of combustion chamber. J. Propul. Power **32**(5), 1087–1094 (2016). https://doi.org/10.2514/1.B35973
42. Ishimoto, S., Tatiossian, P., Dumont, E.: Overview of the callisto project. In: 32nd ISTS and NSAT (2019). https://elib.dlr.de/132886/
43. Kimura, T., Hashimoto, T., Sato, M., Takada, S., Moriya, S.-I., Yagishita, T., Naruo, Y., Ogawa, H., Ito, T., Obase, K., Ohmura, H.: Reusable rocket engine: firing tests and lifetime analysis of combustion chamber. J. Propul. Power **32**, 1–8 (2016). https://doi.org/10.2514/1.B35973
44. Spalart, P.R., Allmaras, S.R.: A One-Equation Turbulence Model for Aerodynamic Flows. AIAA Paper AIAA-92-0439 (1992) https://doi.org/10.2514/6.1992-439
45. Menter, F.R.: Two-equation eddy-viscosity turbulence models for engineering applications. AIAA J. **32**(8), 1598–1605 (1994). https://doi.org/10.2514/3.12149
46. Rumsey, C.L.: In: Eisfeld, B. (ed.) Application of Reynolds Stress Models to Separated Aerodynamic Flows, pp. 19–37. Springer, Cham (2015). https://doi.org/10.1007/978-3-319-15639-2_2
47. Cécora, R.-D., Radespiel, R., Eisfeld, B., Probst, A.: Differential reynolds-stress modeling for aeronautics. AIAA J. **53**(3), 739–755 (2015). https://doi.org/10.2514/1.J053250
48. Gerlinger, P., Moebius, H., Brueggmann, D.: An implicit multigrid method for turbulent combustion. J. Comput. Phys. **167**(2), 247–276 (2001). https://doi.org/10.1006/jcph.2000.6671
49. Gordon, S., McBride, B.J.: Computer Program for Calculation of Complex Chemical Equilibrium Compositions and Applications. Technical report, NASA Reference Publication 1311 (1996)
50. Bouarfa, M., Bourgoing, A., Carrat, J., Puech, D., Jubera, M., Brenner, P.: Cfd retro-propulsion simulation with flusepa code. In: 56th 3AF International Conference on Applied Aerodynamics (2022)
51. Bykerk, T., Karl, S.: Preparatory cfd studies for subsonic analyses of a reusable first stage launcher during landing within the retpro project. In: EUCASS, CEAS (eds.) 10th EUCASS–9th CEAS Conference 2023, pp. 1–10 (2023). https://elib.dlr.de/194477/
52. Eça, L., Hoekstra, M., Hay, A., Pelletier, D.: A manufactured solution for a two-dimensional steady wall-bounded incompressible turbulent flow. Int. J. Comput. Fluid Dynam. **21**(3–4), 175–188 (2007). https://doi.org/10.1080/10618560701553436
53. Standard Atmosphere, U.S.C.: US Standard Atmosphere, 1976. National Oceanic and Amospheric Administration, Chichester (1976)
54. Sagliano, M., Tsukamoto, T., Hernandez, J.A.M., Seelbinder, D., Ishimoto, S., Dumont, E.: Guidance and control strategy for the callisto flight experiment. In: 8th European Conference for Aeronautics and Space Sciences (EUCASS), Madrid (2019). https://elib.dlr.de/128999/